Batteries & Supercaps

Research Article
doi.org/10.1002/batt.202200385

Chemistry Europe
European Chemical Societies Publishing

www.batteries-supercaps.org

Special Collection

Electron Storage Performance of Hybrid Materials Comprising Polyoxometalates and Carbon Nanohorns as Cathode-Active Materials

Katsuhiro Wakamatsu,*[a, b] Akinori Sekihara,[a] Yoshihiko Yamaguchi,[a] Ryo Matsushima,[a] Daiju Matsumura,[c] Tapas Kuila,[d] and Hirofumi Yoshikawa*[a]

Nanohybrid materials comprising polyoxometalates (POMs) and nanocarbons have attracted considerable attention as electrode-active materials for rechargeable lithium-ion batteries (LIBs). These materials exhibit multi-electron redox reactions, resulting in an improved battery capacity. This study focuses on carbon nanohorns (CNHs) as a nanocarbon material and evaluates the battery performance using POM/CNH hybrids as cathode-active materials. X-ray absorption fine structural analysis was performed to investigate the reaction mechanism of these hybrids. POM/oxidized CNH (CNHox) hybrid materials maintain high capacities at high current densities as the high surface area availability of CNHox leads to high electrical double-layer capacitances. These findings show an improved performance of the as-developed material when compared with those reported in previous papers and can contribute toward an improved design of cathode-active materials for high-performance supercapacitors.

Introduction

Currently, severe energy and environmental issues, such as fossil fuel depletion and global warming, are major concerns worldwide. Lithium-ion batteries (LIBs) are potential high-performance energy-storage devices that can address these issues. However, the existing LIBs, comprising a graphite anode and transition metal oxides ($LiCoO_2$) as the cathode, exhibit only 50% of the theoretical capacity because the crystal structure of $LiCoO_2$ is unstable when more than half of the Li^+ ions are removed during the charging process.[1] The application of LIBs are hindered by additional issues, including slow charge/discharge rates and the use of expensive and toxic Co elements. Therefore, improving the performance of LIBs remains an important research topic. The development of environmentally friendly electrode materials with high battery capacity is essential for industrial applications, such as portable electronic devices, electric vehicles, and power grids.[2]

Recently, organic-inorganic hybrid materials have been extensively researched as alternative materials to conventionally used battery materials.[3] Organic-inorganic materials are inexpensive and environmentally friendly because they do not contain transition metals, such as cobalt oxides. Thus far, our group has focused on multinuclear metal coordination compounds with multi-redox reactions, such as Mn12[4,5] and polyoxometalate (POM),[6–8] as organic-inorganic hybrid materials. In particular, Keggin-type POM clusters have attracted attention owing to their ability to undergo 24 multi-electron redox reactions, leading to an improved battery capacity.[6–8] Furthermore, we performed nanohybridization between POM and nanocarbons, wherein all POM cluster molecules were independently bonded to nanocarbons, such as single-walled carbon nanotubes (SWCNTs)[9,10] and conductive agents, such as reduced graphene oxides (RGOs).[11,12] Nanohybridization induces effective electron transfer to POM via nanocarbons, effectively diffuse and retain Li^+ ions from the electrolyte, and improves capacitance owing to the electrical double layer capacitance (EDLC) of nanocarbons, leading to a higher capacity and an improved charge/discharge rate. Nanocarbons with higher surface areas have correspondingly higher EDLCs, which improve the pseudo-capacitance of these nanohybrid materials. This indicates that the use of nanocarbons with an even larger surface area may result in higher capacities when subjected to high current densities. Therefore, hybridization with nanocarbons increases their original EDLCs.

Herein, we selected carbon nanohorns (CNHs) as the nanocarbon material, as they exhibit good electrical conductivity, stable mechanical strength, large surface areas, and more

[a] Dr. K. Wakamatsu, A. Sekihara, Y. Yamaguchi, R. Matsushima, Prof. H. Yoshikawa
Graduate School of Science and Technology
Kwansei Gakuin University
1 Gakuen Uegahara, Sanda, Hyogo 669-1330, Japan
E-mail: yoshikawah@kwansei.ac.jp
katsu29yukke@gmail.com
Homepage: https://researchmap.jp/K.Wakawatsu
[b] Dr. K. Wakamatsu
Department of Chemical Engineering
Massachusetts Institute of Technology
Cambridge, Massachusetts 02139, United States of America
[c] Dr. D. Matsumura
Materials Sciences Research Center
Japan Atomic Energy Agency
Tokai, Ibaraki 319-1195, Japan
[d] Dr. T. Kuila
Surface Engineering and Tribology Division
Council of Scientific and Industrial Research-Central Mechanical Engineering Research Institute
Mahatma Gandhi Avenue, Durgapur 713209, India

Supporting information for this article is available on the WWW under https://doi.org/10.1002/batt.202200385

An invited contribution to a Special Collection on Organic Batteries

Research Article
doi.org/10.1002/batt.202200385
Chemistry Europe
European Chemical Societies Publishing

active sites, to explore the performance of POM hybrid materials in comparison to alternative bonding configurations (SWCNT and RGO).[13–16] In particular, we used as-grown CNH (CNHag)[16–19] and oxidized CNH (CNHox), which are expected to further increase the surface area and allow direct access to the inner structure owing to the aperture treatment at the tip.[17,19–21] Herein, we synthesized POM/CNH hybrid materials and evaluated their electron storage performance in terms of their charging/discharging functionality at high current densities using electrochemical measurements. We also attempted to reveal the electrochemical redox reaction mechanism using X-ray absorption fine structure (XAFS) analysis.

Results and Discussion

First, the structures of hybrid materials comprising POM and CNHs were characterized. Figures 1(a–d) and S1 show transmission electron microscopy (TEM) images of CNHag, POM/CNHag hybrids, CNHox, and POM/CNHox hybrids and Mo mapping using scanning electron microscopy with energy dispersive X-ray spectroscopy (SEM-EDX) images of POM/CNHag and POM/CNHox hybrids, respectively. TEM images in Figure 1(b and d) show particles with an approximate diameter of 1.1 nm on CNHag and CNHox.[16–19] The POM molecule diameter was approximately 1.5 nm.[9] Mo atoms were observed in the SEM-EDX images as shown in Figure S1(a and b). Fourier transformed Mo *K*-edge extended X-ray absorption fine structure (EXAFS) spectra of nanohybrid materials are also consistent with that of the POM as shown in Figure S2. These results suggest that POM is adsorbed on CNHag and CNHox in single to multi-molecular units, forming POM/CNHag and POM/CNHox hybrid materials since Anionic $[PMo_{12}O_{40}]^{3-}$ ions are assumed electrostatically attracted to the organic ammonium cations on CNHag and CNHox .[9] Unlike the case of CNHag, there are some possibilities that POM was inserted into CNHox to form POM/CNHox hybrid materials since the tip of CNHox was opened.[19,20]

Figure 2 shows the Raman spectra of CNHag, CNHox, and their hybrid materials with POM. The Raman spectra of all materials exhibit peaks at approximately 1580 (G band) and 1350 cm^{-1} (D band).[22] The intensity ratios of the D and G bands (I_D/I_G) for both CNHs and POM hybrid materials are listed in Table S1. The I_D/I_G values in Table S1 for both CNHs agree with those reported in previous papers (CNHag: 0.91, CNHox: 1.43);[23] the I_D/I_G value for CNHox is larger than that for CNHag, indicating a higher number of nanopores and defects in the CNHox.[24] Additionally, the I_D/I_G values of CNHag and CNHox remained almost unchanged after hybridization with POM. This indicates that no specific structural changes occurred during the fabrication of the hybrid materials. Peak deconvolution of Raman spectra for CNHag, CNHox, POM/CNHag, and POM/CNHox was performed according to the literatures[25,26] as shown in Figure S3. D and G main peaks were observed for all materials with I and D'' peaks although D' peaks were not observed: G, D, and I peaks correspond to the in-plane vibration of the sp^2 carbon atom which means the ordered graphitic layers, the vibration of carbon atoms at the surface defect and/or edges of the graphite layers which means the disordered graphitic structures, and the disorder in the graphitic lattice or the presence of polyenes, while D'' and D' peaks are assigned to the existence of amorphous carbon and the defect induced peak associated with the disorder in graphene, respectively.[25,26] This indicates that CNHag and CNHox have a relatively pure state even after hybridization with POM.

Figure S4 shows the X-ray photoelectron spectroscopy (XPS) profiles of the POM/CNHox hybrid material; the C 1s and O 1s peaks are at approximately 285 and 532 eV, respectively, and the Mo 3d peaks are at approximately 233 and 236 eV. The N 1s and P 2p peaks were observed at approximately 532 and 134 eV. The Mo 3d and P 2p peak positions were consistent with those in the previously reported XPS profiles of POM.[27] This indicates that the Mo 3d and P 2p peaks result from the

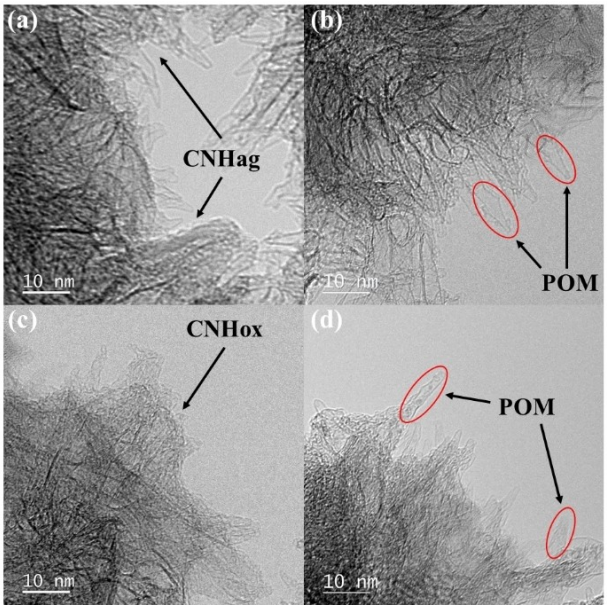

Figure 1. TEM images of a) CNHag, b) POM/CNHag hybrid materials, c) CNHox, and d) POM/CNHox hybrid materials.

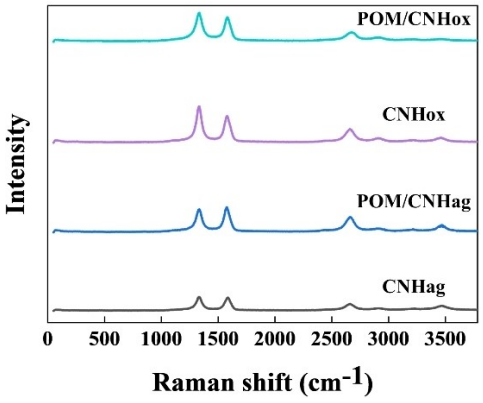

Figure 2. Raman spectra of CNHag, CNHox, and their hybrid materials with POM.

Research Article
doi.org/10.1002/batt.202200385
Chemistry Europe
European Chemical Societies Publishing

presence of POM molecules, suggesting that the electronic structure of the POM molecules does not change after nanohybridization with CNHox. Herein, the C 1s, O 1s, and N 1s peaks are assigned to CNHox, POM molecules, and tetrabutylammonium (TBA) molecules used as POM countercations, respectively. The results suggest that well-formed POM/CNHox hybrid materials can be produced using the proposed preparation method. Considering that the surface area of CNHox (1300–1400 m^2/g[28]) is larger than that of CNHag (400 m^2/g[28]) and that easier Li^+ ion diffusion in CNHox is probably caused by aperture treatment at the tip of the CNH, it is expected that the POM/CNHox hybrid materials will exhibit better battery performance.

We first evaluated the battery performance of the POM/CNHox hybrid material. The charge-discharge curves of the POM/CNHox hybrid material at a current density of 500 mA/g are shown in Figure 3(a). Herein, we present the second and third charge-discharge curves as representative curves because the first discharge curve differs from the others, probably owing to the insufficient insertion of Li ions in the first cycle possibly caused by the structure of CNHox. Figure 3(a) shows that the POM/CNHox hybrid material battery exhibits a plateau near 3.0 V. A maximum capacity of 508 mAh/g is observed in the second discharge process, which is higher than that of the POM-only materials (281 mAh/g) and POM-hybrid materials with other nanocarbons (CNHag: 332 mAh/g, RGO: 431 mAh/g, and SWCNT: 360 mAh/g) (see Figure S7 and Table S2). Figure 3(b) shows the cycle dependence of the discharge capacity and Coulombic efficiency of the POM/CNHox hybrid material at a current density of 500 mA/g. Coulombic efficiency is maintained above 90% after 30 cycles; a gradual decrease in capacity was observed after cycling (the discharge capacity retention rate was 48% after 100 cycles, see Table S4). It is considered that the gradual capacity decrease is induced by the solution of active materials into the electrolyte. When the current density increased to 1000 mA/g, the maximum discharge capacity was approximately 468 mAh/g during the second discharge process, which is also higher than those of POM materials (274 mAh/g) and POM hybrids with other nanocarbons (CNHag: 301 mAh/g, RGO: 402 mAh/g, and SWCNT: 324 mAh/g) (see Figure S9 and Table S2). In particular, the maximum discharge capacity during the second discharge process at a current density of 1000 mAh/g was larger than that of the POM/CHNox hybrid at a current density of 200 mAh/g during the second discharge. Generally, battery capacity decreases with an increase in current density.[29,30] This result indicates that unlike POM materials hybridized with SWCNT and RGO, the POM/CNHox hybrid materials can maintain a high battery capacity even at high current densities and have the potential for achieving improved charging/discharging rates. This is because CNHox has a higher specific surface area when compared with other nanocarbons (CNHox: 1300–1400 m^2/g,[28] CNHag: 400 m^2/g,[28] RGO: 450 m^2/g,[31] and SWCNT: 400–1000 m^2/g[32]) and easier Li^+ ion diffusion was induced by aperture treatment at the tip of CNHox. The charge-discharge curves and the cycle dependence of the discharge capacities and coulombic efficiency of other nanocarbons and hybrid materials at current densities of 200, 500, and 1000 mA/g are shown in Figures S5 and S6, Figures S7 and S8, and Figures S9 and S10, respectively. Moreover, the maximum and minimum discharge capacities and discharge capacity retention rates of POM, nanocarbons, and POM/nanocarbon hybrid batteries at current densities of 200, 500, and 1000 mA/g are summarized in Tables S2, S3, and S4, respectively.

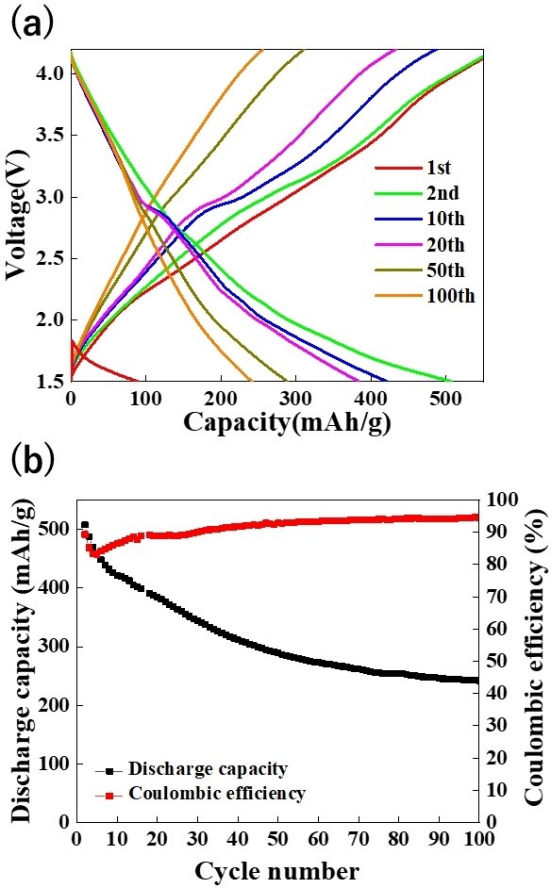

Figure 3. a) Charge-discharge curves and b) cycle dependence of the discharge capacities and coulombic efficiency for the POM/CNHox hybrid material at a current density of 500 mA/g.

The cyclic voltammetry (CV) profile of the POM/CNHox hybrid battery is shown in Figure 4. This figure shows that small, sharp peaks are observed at approximately 2.5–3.0 V, which is consistent with the plateau observed at 2.0–3.5 V in Figure 3(a), suggesting that the redox reaction occurs stepwise within this voltage range (2.5–3.0 V); this is reasonable for battery measurements. Multiple peaks indicate that multi-electron redox reactions occur in the POM/CNHox hybrid because POM has 12 Mo sites. In addition, the CV profile of the hybrid material shows a rectangular curve, indicating that the hybrid material exhibits a pseudo-capacitor-like behavior. The CV profiles of other nanocarbons and hybrid materials are shown in Figures S11 and S12.

The charge-discharge curves and the cycle dependence of the discharge capacities and coulombic efficiency of the POM/CNHox hybrid material at a current density of 500 mA/g while

Research Article
doi.org/10.1002/batt.202200385
Chemistry Europe
European Chemical Societies Publishing

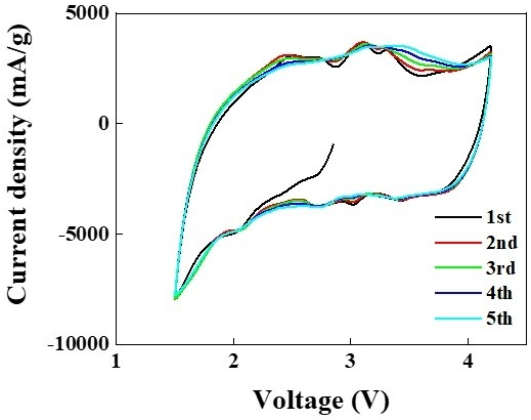

Figure 4. CV profile for the POM/CNHox hybrid material.

using 1.0 M lithium bis(trifluoromethanesulfonyl)imide (LiTFSI) in a 1-butyl-3-methylimidazolium bis(trifluoromethylsulfonyl)imide (BMImTFSI) electrolyte solution are shown in Figure 5(a and b). The highest discharge capacity is 392 mAh/g (Figure 5), which is lower than that of 1.0 M $LiPF_6$ in ethylene carbonate (EC):diethyl carbonate (DEC) = 1:1 in the weight ratio

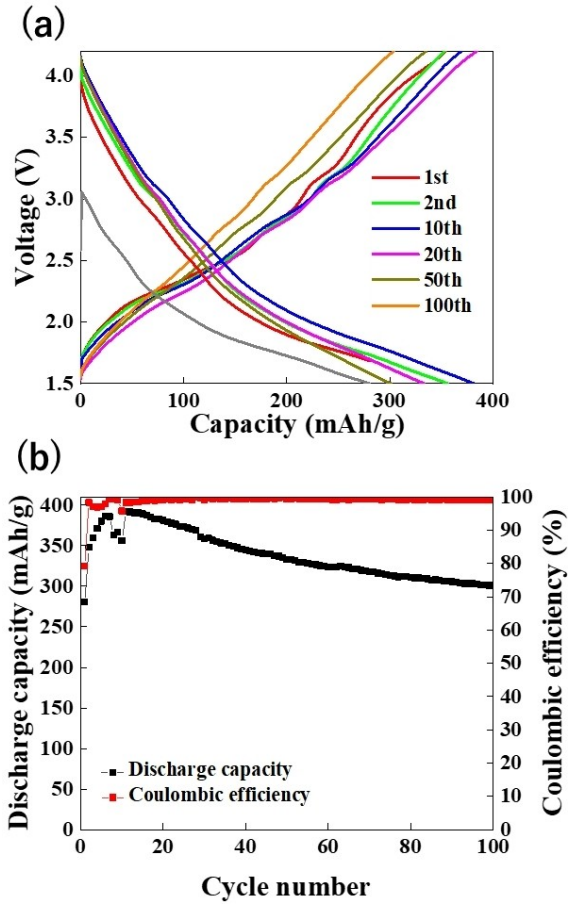

Figure 5. a) Charge-discharge curves and b) cycle dependence of the discharge capacities and coulombic efficiency for the POM/CNHox hybrid material at a current density of 500 mA/g while using 1.0 M LiTFSI in BMImTFSI electrolyte.

electrolyte solution at 508 mAh/g. However, Coulombic efficiency is maintained at approximately 100% (the discharge capacity retention rate after 100 cycles was 77%; see Table S4), as shown in Figure 5(b). These are more stable than the case of 1.0 M $LiPF_6$ in EC:DEC = 1:1 in the weight ratio electrolyte solution, with an approximate coulombic efficiency of 92% and a retention capacity of 48% after 100 cycles. This indicates that room temperature ionic liquids (RTILs) improve the service life of POM/CNHox hybrid material batteries, even though the battery capacity is low. The charge/discharge curves and cycle dependence of the discharge capacities and coulombic efficiency of other nanocarbons and hybrids at a current density of 500 mA/g while using 1.0 M LiTFSI in the BMImTFSI electrolyte solution are shown in Figures S13 and S14. The maximum and minimum discharge capacities and discharge capacity retention rates of only POM, only nanocarbons, and POM/nanocarbon hybrid batteries are summarized in Tables S2, S3, and S4, respectively, while using 1.0 M LiTFSI in BMImTFSI electrolyte solution at a current density of 500 mA/g.

The electrochemical impedance spectroscopy (EIS) profiles of the POM and POM/nanocarbon hybrid materials are shown in Figure 6. The charge-transfer resistance value of the POM (194 Ω) is in agreement with previously reported values in literature (approximately 240 Ω).[8] As shown in Figure 6, all charge-transfer resistances of POM after hybridization (CNHag: 147 Ω, CNHox: 66 Ω, RGO: 83 Ω, and SWCNT: 111 Ω) are lower than the charge-transfer resistance of POM alone as an insulator, which implies that the nanohybridization method is a suitable method for improving charge conductivity. This method allows for sufficient POM reduction and high battery capacities. Additionally, the charge-transfer resistance of the POM/CNHox hybrid material was the smallest compared to that of other POM/nanocarbon hybrid materials, as CNHox has the highest surface area, which explains the high capacities of the POM/CNHox hybrid material even when exposed to high current densities.

To reveal the reaction mechanism, we performed operando Mo *K*-edge X-ray absorption near-edge structure (XANES) spectroscopy of the POM/CNHox hybrid material. Figure S15(a) shows the charge/discharge curves during the operando XAFS

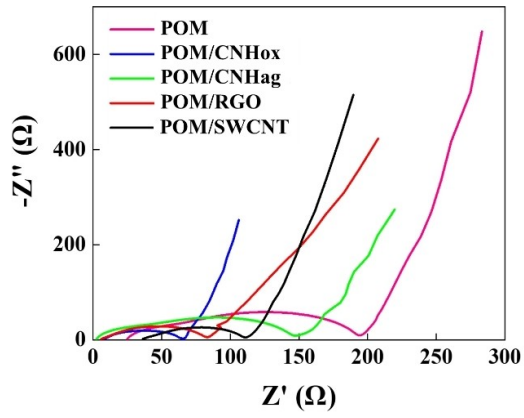

Figure 6. EIS profiles of POM and POM/nanocarbon hybrid materials.

Research Article
doi.org/10.1002/batt.202200385
Chemistry Europe
European Chemical Societies Publishing

measurements of the POM/CNHox hybrid materials at a current density of 100 mA/g. The second discharge capacity was 417 mAh/g; the behavior was similar to that of the coin cell battery shown in Figure 3(a). The normalized operando Mo *K*-edge XANES spectrum of the POM/CNHox hybrid is shown in Figures 7 and S15(b), which suggest large spectral changes during the charge/discharge processes. Specifically, the absorption edges shifted to the high-energy side during the charging process and to the low-energy side during the discharging process. This indicates that the spectral changes are reversible during the charge/discharge process. A low-intensity peak was observed at approximately 20,010 eV in the pre-edge region. This peak appears during the charging process and disappears during the discharging process. This result is affected by a formally dipole forbidden excitation from the 1 s to 4d antibonding orbitals directed principally along the Mo=O bond, indicating that the appearance and disappearance of this small peak are induced by the formation and elimination of Mo=O bonds, respectively.[6,33,34] Mo *K*-edge XANES absorption edge energies can be used to estimate the Mo valences using a linear relationship between the Mo oxidation states and the absorption edge energy of the reference samples (MoO_2 and MoO_3). The edge energy is defined as the point at which the intensity reaches approximately 70% of that of the absorption peak in this study.[6,35–37] The change in the average Mo valences as a function of the battery voltage, estimated using the edge energies in Figure 7, are shown in Figure 8. The value of Mo valences decreases from approximately 6.0 to 4.0 during the discharge process and then recovers to 6.0 during the charging process; the average Mo valence change is 2.0 (with a reversible tendency during charge/discharge processes). Mo valences do not significantly change in the voltage range between 3.0 and 4.0 V; however, a notable change occurs in the voltage range of 1.5–3.0 V. This change in the voltage range agrees with the theoretical battery voltages (2.0–3.5 V) calculated from the redox potentials of $[PMo_{12}O_{40}]^{3-}$.[6,38] This result indicates an approximately 24-electron reduction per POM molecule, and the super-reduction state $[PMo_{12}O_{40}]^{27-}$, which cannot be observed in solutions in electrochemistry (approximately 2–4 electron redox), is produced in battery reactions, such as solid-state electrochemistry,[38–40] which is also known as electron sponge function.[6,41,42]

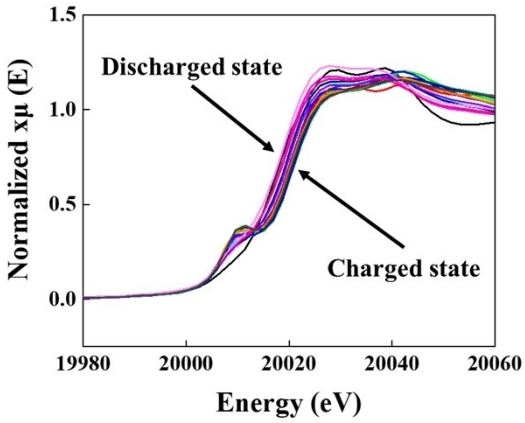

Figure 7. *In situ* Mo *K*-edge XANES spectra of a POM/CNHox hybrid material battery.

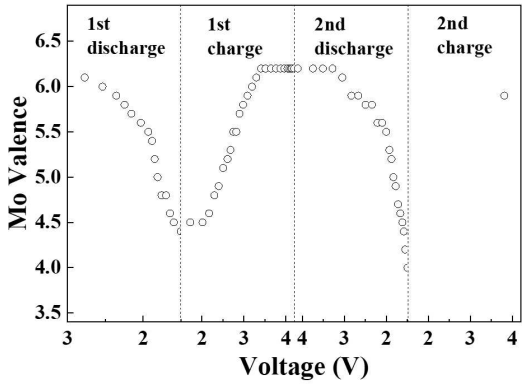

Figure 8. Averaged Mo valence of the POM/CNHox hybrid material battery as a function of cell voltage.

The XANES results indicate that the experimental capacities of hybrid materials cannot be explained using the redox reaction of POM in hybrids alone, as the theoretical redox capacity of POM is ~252 mAh/g, under the assumption that a redox reaction of 24 electrons per molecule occurs. Therefore, the nanocarbons contribute to the EDLC of hybrid materials.[11,12,43] Finally, we estimated the EDLC values of the POM/CNHox hybrid materials. Table 1 summarizes the capacities of POM, nanocarbons, and POM/nanocarbon hybrid materials at current densities of 200, 500, and 1000 mA/g. The battery capacity of CNHox is 78 mAh/g at a current density of 500 mA/g, which indicates that the excess capacity of the POM/CNHox hybrids, except for the POM redox capacity (175 mAh/g at a current density of 500 mA/g), cannot be explained using the electron storage effect (EDLC) of CNHox. The increased capacitances of the nanohybrid materials are summarized in Table 2. Here, the increased capacities were calculated according to the following equation: enhanced capacity = (POM/nanocarbon hybrid materials) – (only POM + 2/3 × only nanocarbons). In all POM/nanocarbon hybrid materials, a significant contribution other than that from POM (i.e., EDLC) is observed. The increased capacity of the POM/CNHox hybrids at a current density of 500 mA/g is the highest, and this excess capacity can

Table 1. Maximum discharge capacities of only POM, only nanocarbon, and POM/nanocarbon hybrid material batteries at a current density of 200, 500, and 1000 mA/g. Note that (a)–(d) are 6th, 4th, 7th, and 3rd cycle values, respectively. Others are 2nd cycle values.

Materials	Maximum discharge capacity [mAh/g]		
	at 200 mA/g	at 500 mA/g	at 1000 mA/g
POM	288[(a)]	281[(b)]	274[(b)]
CNHag	76	71	66[(c)]
CNHox	86	78	71
RGO	116	113	96
SWCNT	106	92	91
POM/CNHag	307	332	301
POM/CNHox	368	508	468
POM/RGO	433	431	402
POM/SWCNT	389	360[(d)]	324[(d)]

Research Article
doi.org/10.1002/batt.202200385
Chemistry Europe
European Chemical Societies Publishing

Table 2. Pseudo-capacities of POM/nanocarbon hybrid material batteries.

Hybrid materials	Pseudo-capacities [mAh/g] at 200 mA/g	at 500 mA/g	at 1000 mA/g
POM/CNHag	−32	4	−17
POM/CNHox	23	175	147
POM/RGO	67	75	64
POM/SWCNT	30	18	−11

be attributed to the EDLC effect owing to hybridization and the high specific surface area of the CNHox. Considering the aforementioned data and findings, POM/CNHox hybrids exhibit a higher performance compared with previously reported POM/nanocarbon hybrid materials owing to the super-reduction of POM and the increased EDLC values due to nanohybridization based on the higher surface area of CNHox, resulting in a high pseudo-capacitance even at high current densities. We also think that cycling performances in capacity during charging/discharging processes can be improved by preventing active materials from dissolving into electrolytes, through the adoption of suitable electrolytes and the development of insoluble hybrid materials by chemical modifications. In next, it is exhibited that RTILs improved the cycling performance of almost hybrid material batteries, even though the battery capacity is low (see Figures S13 and S14; and Tables S1–S3).

Conclusion

In summary, we prepared POM/CNHox hybrid materials as cathode-active electrode materials for Li-ion rechargeable batteries. The POM/CNHox hybrid materials maintain a high battery capacity even at high current densities in the galvanostatic charge/discharge tests, and the observed capacity was higher than those of POM/nanocarbon hybrid materials reported in previous literature. Additionally, *in situ* Mo *K*-edge XAFS analysis revealed reversible electrochemical redox mechanisms of POM with two electrons per Mo atom in the POM/CNHox hybrids during the charge/discharge process. Finally, owing to the super-reduction of POM and the increase of EDLC by nanohybridization with CNHox bearing the higher surface area, POM/CNHox hybrid materials exhibit a higher pseudo-capacitance. This is caused by unique structural features of CNHox, of which the outside and inside surfaces can be used for EDLCs. Therefore, it is suggested that nanohybridization with nanocarbon bearing a higher surface area and specific structures is an effective method for realizing high-performance energy storage devices. We believe that our findings will facilitate the development of active electrode materials for next-generation rechargeable batteries and direct the attention of the battery research community toward the possible application of POM hybridization materials as active electrode materials.

Experimental Section

Material preparation

Keggin-type POM, $TBA_3[PMo_{12}O_{40}]$, was prepared as follows: First, 1.93 g (6 mmol) $(C_4H_9)_4NBr$ (Wako) in 10 mL solution was added to 3.65 g (2 mmol) $H_3PMo_{12}O_{40}$ (Aldrich) dissolved in 20 mL water, leading to the precipitation of a yellow solid. Next, the solid was suction-filtered, washed with water, ethanol, and diethyl ether (in that order), and then recrystallized with acetone to obtain Keggin-type POM. The POM/nanocarbon hybrid materials were prepared using the following steps. Here, the weight ratio of POM:nanocarbon was 1:2, and the nanocarbons were assumed to be CNHag (NEC),[16–19] CNHox (NEC),[17,19–21] RGO (Sigma-Aldrich),[11,12] or SWCNT (Opto Science),[9,10] for comparison. First, nanocarbons (100 mg) were finely ground in a mortar to prepare a dispersion solution with toluene (75 mL) and sonicated for 30 min. Thereafter, an acetonitrile solution (5 mL) of POM (50 mg) was slowly added dropwise to the toluene dispersion solution for approximately 30 min while continuing the sonication. Finally, the dispersion solution was suction-filtered and vacuum-dried for fabricating POM/nanocarbon hybrid materials.

TEM analysis

TEM was performed on a JEM-2200FS (JEOL) instrument; the accelerating voltage was set to 200 kV. The samples were dissolved in hexane and dropped onto the grid after dispersion via ultrasonication. The excess liquid was then removed using filter paper and dried for observation.

SEM-EDX analyses

SEM-EDX was performed on a FlexSEM 1000 (HITACHI) system, and the voltage was set to 15 kV. The samples on the carbon tapes were sputtered with gold in a vacuum for 2 min, and then, SEM images of the samples were taken under high vacuum conditions.

Raman spectroscopy analysis

Raman spectroscopy (3784–50 cm^{-1}) was performed on an NRS-4100 (JASCO) system equipped with a 532 nm laser. Measurements were performed using a 10×1000 μm slit and 600 mm^{-1} gratings, with an aperture ϕ of 4000 μm, an OD2 attenuator with an exposure time of 60 s (or OD2 attenuator with an exposure time of 180 s), the integration of two times, and a magnification of 100.

XPS analysis

XPS was performed on an ESCALAB Xi^+ instrument (Thermo Fisher Scientific Pvt. Ltd., UK) equipped with an Al Kα source under ultrahigh vacuum conditions ($\leq 5\times10^{-10}$ mbar).

Battery fabrication

The cathode was fabricated as follows: First, POM/nanocarbons (CNHag, CNHox, RGO, or SWCNT), hybrid materials (the weight ratio of POM:nanocarbons = 1:2), and Toka Black #5500 (Tokai Carbon) were ground using an agate mortar and a pestle for 30 min. The polyvinylidene fluoride (PVDF) binder (#1100, Kishida Chemical) was then added, and the mixture was ground again for 30 min. As shown in Figure S16, the weight ratio of the POM:nanocarbon hybrid materials, Toka Black #5500, and PVDF was 30:50:20. Note that the weight ratio of POM:Toka Black #5500:PVDF = 1:7:2 and

the weight ratio of nanocarbon:Toka Black #5500:PVDF = 3:5:2 were used in the case of only POM and nanocarbon materials, respectively. Next, a slurry was prepared by adding anhydrous *N*-methylpyrrolidone (NMP) (Sigma-Aldrich) to the mixture. The mixed slurry was cast onto an aluminum foil (thickness: 20 μm) using the doctor blade technique and dried overnight in a vacuum. Finally, the aluminum foil coated with the slurry was cut into disks (diameter ϕ = 15.95 mm) as active electrode materials. CR2032 coin-type cells were assembled in an Ar-filled glovebox using the prepared materials as the cathode and lithium foil (thickness: 0.2 mm, ϕ: 15.50 mm) as the anode. A polypropylene separator was used to prevent the dissolution of active materials, and 1.0 M $LiPF_6$ in EC:DEC = 1:1 in the weight ratio solution (Kishida Chemical) was used as the electrolyte to avoid undesirable side reactions. These CR2032 coin-type cells were used in galvanostatic tests, CV experiments, and EIS. For comparison, in the galvanostatic tests, 1.0 M LiTFSI in BMImTFSI solution, which is an RTIL electrolyte, was used as the electrolyte for assembling CR2032 coin-type cells.

Preparation of 1.0 M LiTFSI in BMImTFSI

This electrolyte was prepared as follows: 1.0 M LiTFSI (Wako) was dissolved in BMImTFSI (> 98%, Wako) and maintained undisturbed for 4 days with occasional stirring in an Ar-filled glove box.[44]

Galvanostatic charge/discharge tests

Galvanostatic charge/discharge tests were performed on an HJ102mSD8 (HOKUTO DENKO) system at room temperature (approximately 25 °C). The cells were cycled at 200, 500, and 1000 mA/g for the weight of active material between 1.5 and 4.2 V (vs. Li^+/Li).

CV experiments

The CV experiments are performed on an HZ-Pro S12 (HOKUTO DENKO) system over the voltage range of 1.5–4.2 V at a scan rate of 0.2 mV/s at room temperature (approximately 25 °C).

EIS analysis

EIS measurements were performed on an HZ-Pro S12 (HOKUTO DENKO) system, where the start and end frequencies were 100 kHz and 10 mHz, respectively.

In situ Mo *K*-edge XAFS

The *in situ* Mo *K*-edge XAFS measurements (19,980–20,060 eV) were performed in the transition mode at room temperature (approximately 25 °C) using the BL14B1 beamline at SPring-8 (8.0 GeV, 100 mA). The pellet cathode samples used for *in situ* XAFS measurements were employed for electrochemical measurements (the weight ratio of POM:CNHox hybrid materials, Toka Black #5500, and PVDF was 30:50:20). Mo foil, MoO_2 (Aldrich), MoO_3 (Wako), and a POM/CNHox hybrid material diluted with boron nitride (Wako) were used as standard materials. For *in situ* XAFS measurements, a special battery cell (ϕ:150 mm) with a Kapton film X-ray window (ϕ:2 mm) in the center was fabricated according to literature.[5,6] The *in situ* special battery cell was placed between the two transmission ion chambers. X-rays from a bending magnet were monochromatized using a Si (111) double-crystal monochromator. The intensities of the incident (I_0) and transmitted (I_1) X-rays were detected using ion chambers filled with N_2 (100%, I_0 chamber) or N_2/Ar (75/25%, I_1 chamber). The X-ray spot size at the measurement position was adjusted to 1.0 (horizontal) and 0.8 mm (vertical) using a slit. Galvanostatic charge/discharge tests during *in situ* XAFS measurements were performed at room temperature on an HJ102mSD8 (HOKUTO DENKO) system. The special battery cell is cycled at 100 mA/g for the weight of active material between 1.5 and 4.2 V (vs. Li^+/Li). XAFS profiles were obtained every 20 min. EXAFS and XANES analysis were performed by using the Athena software.

Acknowledgements

We acknowledge the financial support provided by the Japan Society for the Promotion of Science (JSPS) KAKENHI Grant-in-Aid for Challenging Research (Exploratory) (Proposal No. 19K22222), JSPS KAKENHI Grant-in-Aid for Scientific Research on Innovative Areas (Research in a Proposed Research Area) (Proposal No. 20H04680 and 20H04646), JSPS KAKENHI Grant-in-Aid for Challenging Research (Exploratory) (Proposal No. 22K19073), and Japan-India Science Cooperative Program between the JSPS and Department of Science and Technology (DST) (Proposal No. JPJSBP120207720). This study was also financially supported by the Yazaki Memorial Foundation for Science and Technology, JSPS Core-to-Core Program A-Advanced Research Networks "International Network on Polyoxometalate Science for Advanced Functional Energy Materials", and Collaborative Special Research Subsidy and Individual Research Subsidy (Kwansei Gakuin University, 2021). The synchrotron radiation experiments for Mo K-edge XAFS were performed at the JAEA beamline BL14B1 in SPring-8 with the approval of the Japan Synchrotron Radiation Research Institute (JASRI) (Proposal No. 2021A3634, 2021B3634, and 2022A3634). This study was performed under the Shared Use Program of the Japan Atomic Energy Agency (JAEA) facilities (Proposal Nos. 2021A-E01, 2021B-E01, and 2022A-E01) with the approval of the Nanotechnology Platform (NTP) (Synthesis of Molecules and Materials) (Proposal No. JPMXP09A21AE0001 and JPMXP09 A21AE0024) and advanced research infrastructure for materials (ARIM) projects supported by the Ministry of Education, Culture, Sports, Science, and Technology (MEXT), Japan (Proposal No. JPMXP1222AE0001). The TEM and Raman spectroscopy measurements were conducted at the Nara Institute of Science and Technology (NAIST), supported by the NTP and ARIM projects of MEXT, Japan. In particular, these measurements were performed by Prof. Kawai Tsuyoshi, Dr. Sakiko Fijita, and Dr. Yasuo Okajima of the Division of Materials Science in NAIST upon discussion with the authors. We also acknowledge the financial support of the Trial Use of Molecule and Material Synthesis (M&MS) Platform (Young Researcher Bracket) of the NTP and ARIM projects supported by MEXT. Fruitful discussion and cooperative support with Mr. Soichiro Furuno of the Graduate School of Science and Technology in Kwansei Gakuin University is also greatly appreciated. Furthermore, we would like to thank Editage (www.editage.com) for English language editing.

Conflict of Interest

The authors declare no conflict of interest.

Data Availability Statement

Research data are not shared.

Keywords: carbon nanohorns · cathode-active materials · electron transfer · polyoxometalates · lithium-ion battery · redox chemistry · X-ray absorption spectroscopy

[1] D. Linden, T. B. Reddy, *Handbook of Batteries*, 3rd ed., McGraw-Hill, New York, **2002**.
[2] B. Dunn, H. Kamath, J.-M. Tarascon, *Science* **2011**, *334*, 928–935.
[3] C. Sanchez, G. J. de A. A. Soler-Illia, F. Ribot, T. Lalot, C. R. Mayer, V. Cabuil, *Chem. Mater.* **2001**, *13*, 3061–3083.
[4] H. Yoshikawa, C. Kazama, K. Awaga, M. Satoh, J. Wada, *Chem. Commun.* **2007**, *43*, 3169–3170.
[5] H. Wang, S. Hamanaka, T. Yokoyama, H. Yoshikawa, K. Awaga, *Chem. Asian J.* **2011**, *6*, 1074–1079.
[6] H. Wang, S. Hamanaka, Y. Nishimoto, S. Irle, T. Yokoyama, H. Yoshikawa, K. Awaga, *J. Am. Chem. Soc.* **2012**, *134*, 4918–4924.
[7] Y. Nishimoto, D. Yokogawa, H. Yoshikawa, K. Awaga, S. Irle, *J. Am. Chem. Soc.* **2014**, *136*, 9042–9052.
[8] H. Wang, T. Yamada, S. Hamanaka, H. Yoshikawa, K. Awaga, *Chem. Lett.* **2014**, *43*, 1067–1069.
[9] N. Kawasaki, H. Wang, R. Nakanishi, S. Hamanaka, R. Kitaura, H. Shinohara, T. Yokoyama, H. Yoshikawa, K. Awaga, *Angew. Chem. Int. Ed.* **2011**, *50*, 3471–3474; *Angew. Chem.* **2011**, *123*, 3533–3536.
[10] H. Wang, N. Kawasaki, T. Yokoyama, H. Yoshikawa, K. Awaga, *Dalton Trans.* **2012**, *41*, 9863–9866.
[11] K. Kume, N. Kawasaki, H. Wang, T. Yamada, H. Yoshikawa, K. Awaga, *J. Mater. Chem. A* **2014**, *2*, 3801–3807.
[12] H. Omachi, T. Inoue, S. Hatao, H. Shinohara, A. Criado, H. Yoshikawa, Z. Syrgiannis, M. Prato, *Angew. Chem. Int. Ed.* **2020**, *59*, 7836–7841; *Angew. Chem.* **2020**, *132*, 7910–7915.
[13] W. Tu, J. Lei, L. Ding, H. Ju, *Chem. Commun.* **2009**, 4227–4229.
[14] C. Cioffi, S. Campidelli, C. Sooambar, M. Marcaccio, G. Marcolongo, M. Meneghetti, D. Paolucci, F. Paolucci, C. Ehli, G. M. A. Rahman, V. Sgobba, D. M. Guldi, M. Prato, *J. Am. Chem. Soc.* **2007**, *129*, 3938–3945.
[15] Y. Zhao, J. Li, Y. Ding, L. Guan, *Chem. Commun.* **2011**, *47*, 7416–7418.
[16] H. Lai, J. Li, Z. Chen, Z. Huang, *ACS Appl. Mater. Interfaces* **2012**, *4*, 2325–2328.
[17] G. Pagona, G. Mountrichas, G. Rotas, N. Karousis, S. Pispas, N. Tagmatarchis, *Int. J. Nanotechnol.* **2009**, *6*, 176–195.
[18] S. Iijima, M. Yudasaka, R. Yamada, S. Bandow, K. Suenaga, F. Kokai, K. Takahashi, *Chem. Phys. Lett.* **1999**, *309*, 165–170.
[19] A. Kagkoura, N. Tagmatarchis, *Nanomater.* **2020**, *10*, 1407.
[20] Y. Nan, B. Li, X. Song, N. Sano, *Carbon* **2019**, *142*, 150–155.
[21] S. Utsumi, J. Miyawaki, H. Tanaka, Y. Hattori, T. Itoi, N. Ichikuni, H. Kanoh, M. Yudasaka, S. Iijima, K. Kaneko, *J. Phys. Chem. B* **2005**, *109*, 14319–14324.
[22] F. Su, J. Zeng, X. Bao, Y. Yu, *Chem. Mater.* **2005**, *17*, 3960–3967.
[23] S. Utsumi, H. Honda, Y. Hattori, H. Kanoh, K. Takahashi, H. Sakai, M. Abe, M. Yudasaka, S. Iijima, K. Kaneko, *J. Phys. Chem. C* **2007**, *111*, 5572–5575.
[24] Y. Nan, Z. Zhang, Y. He, J. Wei, Y. Zhou, *Inorg. Chem.* **2021**, *60*, 16529–16537.
[25] L. Hou, Z. Chen, Z. Zhao, X. Sun, J. Zhang, C. Yuan, *ACS Appl. Energ. Mater.* **2019**, *2*, 548–557.
[26] J. Zhang, D. Wu, Q. Zhang, A. Zhang, J. Sun, L. Hou, C. Yuan, *J. Mater. Chem. A* **2022**, *10*, 2932–2944.
[27] D. Cao, Q. Sha, J. Wang, J. Li, J. Ren, T. Shen, S. Bai, L. He, Y.-F. Song, *ACS Appl. Mater. Interfaces* **2022**, *14*, 22186–22196.
[28] Regent labels (NEC).
[29] F.-C. Shen, C. Guo, S.-N. Sun, Z. Lei, Y.-Q. Lan, *Inorg. Chem.* **2022**, *61*, 11182–11188.
[30] W. Cheng, F.-C. Shen, Y.-S. Xue, X. Luo, M. Fang, Y.-Q. Lan, Y. Xu, *ACS Appl. Energ. Mater.* **2018**, *1*, 4931–4938.
[31] Regent labels (Opto Science).
[32] Regent labels (Sigma-Aldrich).
[33] F. Jalilehvand, B. S. Lim, R. H. Holm, B. Hedman, K. O. Hodgson, *Inorg. Chem.* **2003**, *42*, 5531–5536.
[34] N. R. Shiju, A. J. Rondinone, D. R. Mullins, V. Schwartz, S. H. Overbury, V. V. Guliants, *Chem. Mater.* **2008**, *20*, 6611–6616.
[35] B. Macias, P. Malet, R. Paradinas, V. Rives, M. V. Villa, *Inorg. Chim. Acta* **1999**, *288*, 127–133.
[36] O. V. Safonova, B. Deniau, J.-M. M. Millet, *J. Phys. Chem. B* **2006**, *110*, 23962–23967.
[37] J. Wienold, O. Timpe, T. Ressler, *Chem. Eur. J.* **2003**, *9*, 6007–6017.
[38] K. Maeda, S. Himeno, T. Osaki, A. Saito, T. Hori, *J. Electroanal. Chem.* **1994**, *364*, 149–154.
[39] H. Yoshikawa, *Mol. Sci.* **2013**, *7*, A0061. (Written in Japanese).
[40] H. Yoshikawa, K. Awaga, M. Kamimura, *Catalysts Catalysis* **2014**, *56*, 353–359.
[41] H. Brunner, H. Cattey, W. Meier, Y. Mugnier, A. C. Stückl, J. Wachter, R. Wanninger, M. Zabel, *Chem. Eur. J.* **2003**, *9*, 3796–3802.
[42] M. Bencharif, O. Cador, H. Cattey, A. Ebner, J.-F. Halet, S. Kahlal, W. Meier, Y. Mugnier, J.-Y. Saillard, P. Schwarz, F. Z. Trodi, J. Wachter, M. Zabel, *Eur. J. Inorg. Chem.* **2008**, *12*, 1959–1968.
[43] H. Wang, Z. Zeng, N. Kawasaki, H. Eckert, H. Toshikawa, K. Awaga, *Chem. Eur. J.* **2013**, *19*, 11235–11240.
[44] T. Shimizu, K. Wakamatsu, Y. Yamada, Y. Toyoda, S. Akine, K. Yoza, H. Yoshikawa, *ACS Appl. Mater. Interfaces* **2021**, *13*, 40612–40617.

Manuscript received: August 28, 2022
Revised manuscript received: November 8, 2022
Accepted manuscript online: November 10, 2022
Version of record online: November 24, 2022